

The Thermocline Biases in the Tropical North Pacific and Their Attributions

YUCHAO ZHU,^{a,b,c} RONG-HUA ZHANG,^{a,b,c,d,e} DELEI LI,^{a,b,c} AND DAKE CHEN^{f,g}

^a CAS Key Laboratory of Ocean Circulation and Waves, Institute of Oceanology, Chinese Academy of Sciences, Qingdao, China

^b Center for Ocean Mega-Science, Chinese Academy of Sciences, Qingdao, China

^c Pilot National Laboratory for Marine Science and Technology (Qingdao), Qingdao, China

^d Center for Excellence in Quaternary Science and Global Change, Chinese Academy of Sciences, Xian, China

^e University of Chinese Academy of Sciences, Beijing, China

^f State Key Laboratory of Satellite Ocean Environment Dynamics, Second Institute of Oceanography, Ministry of Natural Resources, Hangzhou, China

^g Southern Marine Science and Engineering Guangdong Laboratory (Zhuhai), Zhuhai, China

(Manuscript received 24 August 2020, in final form 27 October 2020)

ABSTRACT: The tropical thermocline plays an important role in regulating equatorial sea surface temperature (SST); at present, it is still poorly simulated in the state-of-the-art climate models. In this paper, thermocline biases in the tropical North Pacific are investigated using the newly released CMIP6 historical simulations. It is found that CMIP6 models tend to produce an overly shallow thermocline in the northwestern tropics, accompanied by a deep thermocline in the northeastern tropics. A pronounced thermocline strength bias arises in the tropical northeastern Pacific, demonstrating a dipole structure with a sign change at about 8°N. These thermocline biases are accompanied with biases in the simulations of oceanic circulations, including a too weak North Equatorial Countercurrent (NECC), a reduction in water exchanges between the subtropics and the equatorial regions, and an eastward extension of the equatorward interior water transport. The causes of these thermocline biases are further analyzed. The thermocline bias is primarily caused by the model deficiency in simulating the surface wind stress curl, which can be further attributed to the longstanding double-ITCZ bias in the tropical North Pacific. Besides, thermocline strength bias can be partly attributed to the poor prescription of oceanic background diffusivity. By constraining the diffusivity to match observations, the thermocline strength in the tropical northeastern Pacific is greatly increased.

KEYWORDS: Climate models; Model errors; Model evaluation/performance

1. Introduction


Identifying and understanding model biases and further reducing uncertainties are critically important for the assessments of future climate change. Considering the important role played by sea surface temperature (SST) in air–sea interactions, many previous studies have focused on the causes of SST biases and their effects on large-scale atmospheric state (Wang et al. 2014; Richter 2015; Zuidema et al. 2016; Richter and Tokinaga 2020). Subsurface oceans are known to play an important role in the climate system. For example, the acceleration of ocean subsurface warming and the slowdown of surface warming in the early decade of the twenty-first century indicate that deep oceans play an important role in regulating and controlling the global warming (Chen and Tung 2014). Therefore, it is essential to study subsurface biases for understanding the simulations and predictions of global energy and heat redistribution.

The thermocline is an important property in the subsurface ocean, and it is typically defined as the depth with the maximum vertical temperature gradient. By separating the warm upper ocean from the cold deep ocean, thermocline

fluctuation can affect the temperature of seawater entering the upper mixed layer, leading to a variation in SST. For example, equatorial thermocline deepening during the warm phase of El Niño–Southern Oscillation (ENSO) generates warmer water to be pumped into the mixed layer by mean upwelling, leading to an SST warming in the eastern equatorial Pacific (the so-called thermocline feedback during the El Niño events). In addition, with the aid of ventilation process, thermocline anomalies in the subtropics can propagate equatorward, exerting a strong influence on the decadal to interdecadal climate variability in the tropics (Gu and Philander 1997; Zhang et al. 1998). Therefore, vertical displacement of the thermocline is always accompanied by a large change in upper ocean thermal structures, and the thermocline depth simulations in climate models are critical to the realistic simulations of the subsurface ocean.

Despite the important role played by thermocline in regulating the tropical climate, tropical thermocline is poorly simulated in the state-of-the-art climate models (Nagura et al. 2013; Zheng et al. 2016; Castaño-Tierno et al. 2018; Zhang et al. 2020). In general, the thermocline in CMIP5 ensembles is too diffuse and too shallow along the equatorial Pacific (de Szoeke and Xie 2008; Li and Xie 2014) and is too flat and too diffuse along the equatorial Atlantic (Richter et al. 2014; Xu et al. 2014), leading to an unrealistic thermocline feedback in tropical air–sea coupling (Meehl et al. 2001; Xiang et al. 2012; Bellenger et al. 2014).

Thermocline bias in climate models can be traced back to various shortcomings in individual model components. For

 Denotes content that is immediately available upon publication as open access.

Corresponding author: Rong-Hua Zhang, rzhang@qdio.ac.cn

TABLE 1. CMIP6 models used in this study.

No.	Institution	Models
1	Commonwealth Scientific and Industrial Research Organization,	ACCESS-CM2
2	Australian Research Council Centre of Excellence for Climate System Science (CSIRO-ARCCSS)	ACCESS-ESM1-5
3	Alfred Wegener Institute, Helmholtz Centre for Polar and Marine	AWI-CM-1-1-MR
4	Research (AWI)	AWI-ESM-1-1-LR
5	Beijing Climate Center (BCC)	BCC-CSM2-MR
6		BCC-ESM1
7	Chinese Academy of Meteorological Sciences (CAMS)	CAMS-CSM1-0
8	Chinese Academy of Sciences (CAS)	CAS-ESM2-0
9	National Center for Atmospheric Research, Climate and Global	CESM2
10	Dynamics Laboratory (NCAR)	CESM2-FV2
11		CESM2-WACCM
12		CESM2-WACCM-FV2
13	Department of Earth System Science, Tsinghua University (THU)	CIESM
14	Centre National de Recherches Meteorologiques; Centre Europeen	CNRM-CM6-1
15	de Recherche et de Formation Avancee en Calcul Scientifique	CNRM-CM6-1-HR
16	(CNRM-CERFACS)	CNRM-ESM2-1
17	Canadian Centre for Climate Modeling and Analysis, Environment	CanESM5
18	and Climate Change Canada (CCCma)	CanESM5-CanOE
19	Lawrence Livermore National Laboratory; Argonne National	E3SM-1-0
20	Laboratory; Brookhaven National Laboratory; Los Alamos	E3SM-1-1
21	National Laboratory; Lawrence Berkeley National Laboratory;	E3SM-1-1-ECA
	Oak Ridge National Laboratory; Pacific Northwest National	
	Laboratory; Sandia National Laboratories (E3SM-Project)	
22	AEMET; BSC; CNR-ISAC; DMI; ENEA; FMI; Geomar; ICHEC;	EC-Earth3
23	ICTP; IDL; IMAU; IPMA; KIT, Karlsruhe; KNMI; Lund	EC-Earth3-Veg
	University; Met Eireann; NLeSC; NTNU; Oxford University;	
	surfSARA; SMHI; Stockholm University; Unite ASTR; University	
	College Dublin; University of Bergen; University of Copenhagen;	
	University of Helsinki; University of Santiago de Compostela;	
	Uppsala University; Utrecht University; Vrije Universiteit	
	Amsterdam; Wageningen University (EC-Earth-Consortium)	
24	The State Key Laboratory of Numerical Modeling for Atmospheric	FGOALS-f3-L
25	Sciences and Geophysical Fluid Dynamics (LASG), Institute of	FGOALS_g3
	Atmospheric Physics (IAP), Chinese Academy of Sciences (CAS)	
26	First Institute of Oceanography, Ministry of Natural Resources;	FIO-ESM-2-0
	Qingdao National Laboratory for Marine Science and Technology	
	(FIO-QLNM)	
27	National Oceanic and Atmospheric Administration, Geophysical	GFDL-CM4
28	Fluid Dynamics Laboratory (NOAA-GFDL)	GFDL-ESM4
29	Goddard Institute for Space Studies (NASA-GISS)	GISS-E2-1-G
30		GISS-E2-1-G-CC
31		GISS-E2-1-H
32	Met Office Hadley Centre (MOHC)	HadGEM3-GC31-LL
33		HadGEM3-GC31-MM
34	Institute for Numerical Mathematics, Russian Academy of	INM-CM4-8
35	Science (INM)	INM-CM5-0
36	Institut Pierre Simon Laplace (IPSL)	IPSL-CM6A-LR
37	Department of Geosciences, University of Arizona (UA)	MCM-UA-1-0
38	Japan Agency for Marine-Earth Science and Technology; Atmosphere	MIROC-ES2L
39	and Ocean Research Institute, The University of Tokyo; National	MIROC6
	Institute for Environmental Studies; RIKEN Center for	
	Computational Science (MIROC)	
40	Max Planck Institute for Meteorology (MPI-M)	MPI-ESM-1-2-HAM
41		MPI-ESM1-2-HR
42		MPI-ESM1-2-LR
43	Meteorological Research Institute (MRI)	MRI-ESM2-0
44	Nanjing University of Information Science and Technology (NUIST)	NESM3

TABLE 1. (Continued)

No.	Institution	Models
45	Center for International Climate and Environmental Research;	NorCPM1
46	Norwegian Meteorological Institute; Nansen Environmental and	NorESM2-LM
47	Remote Sensing Center; Norwegian Institute for Air Research;	NorESM2-MM
	University of Bergen; University of Oslo and Uni Research (NCC)	
48	Seoul National University (SNU)	SAM0-UNICON
49	Research Center for Environmental Changes, Academia Sinica	TaiESM1
	(AS-RCEC)	
50	Met Office Hadley Centre (MOHC)	UKESM1-0-LL

example, numerical diffusion induced by tracer advection schemes (Tatebe and Hasumi 2010) and misrepresented vertical turbulent mixing (Jochum 2009; Furue et al. 2015; Zhu and Zhang 2018, 2019) in the oceanic models contribute greatly to the diffuse thermocline along the equatorial Pacific. Excessive easterly wind in the central tropical Pacific (Li and Xie 2014) and overestimated subtropical cloud albedo (Burls et al. 2017) in the atmospheric models influence the equatorial thermocline structure through the local oceanic adjustments and the advection of remote temperature biases from the subtropics to the tropics (Thomas and Fedorov 2017), respectively.

Many previous studies have largely focused on the thermocline bias just along the equator. However, little is known about the thermocline simulation in the tropical North Pacific (TNP). The thermocline in the TNP is the crucial precedent source for thermocline variation along the equatorial Pacific and a potential precursor for ENSO evolution (Li et al. 2020). However, our recent study has demonstrated a significant upper-ocean warm bias over the intertropical convergence zone (ITCZ) in the northeastern tropical Pacific, and biases in CMIP6 simulations do not show clear alleviations compared with those in CMIP5 (Zhu et al. 2020), implying that thermocline bias is still rather large and stubborn in the TNP. Although it is substantial, to our surprise thermocline bias in the TNP does not receive a lot of attention yet in climate modeling community.

The thermocline structure is critically important in the TNP, where an upward displacement of ridge-like thermocline exists due to the local wind stress curl-induced Ekman pumping. This thermocline forms a potential vorticity barrier, which acts to block the local water exchange between the subtropics and tropics (Lu and McCreary 1995; Rothstein et al. 1998; Johnson and McPhaden 1999; Zhang and Busalacchi 1999). As such, thermocline bias in the TNP can affect the simulation of subtropical–tropical water exchange and, consequently, affect the simulations of tropical climate (Gu and Philander 1997; Zhang et al. 2001; Lohmann and Latif 2005). Thus in this study, we will focus on the origins and consequences of the TNP thermocline bias using the simulations from CMIP6 models; modeling experiments will be performed to attribute to their causes.

The rest of this paper is organized as follows. Section 2 describes models, datasets, and methods used in this study. Section 3 describes the characteristics of thermocline biases in the TNP. Influences and origins of the thermocline biases are

investigated in sections 4 and 5. Finally, a discussion and summary are given in section 6.

2. Models, datasets, and methods

a. Climate model simulations

This study is primarily based on the historical simulations of the World Climate Research Programme (WCRP) CMIP6 (Eyring et al. 2016), which are available online at <https://esgf-node.llnl.gov/projects/cmip6/>. The historical simulations are forced by the observed solar forcing, volcanic aerosols, and

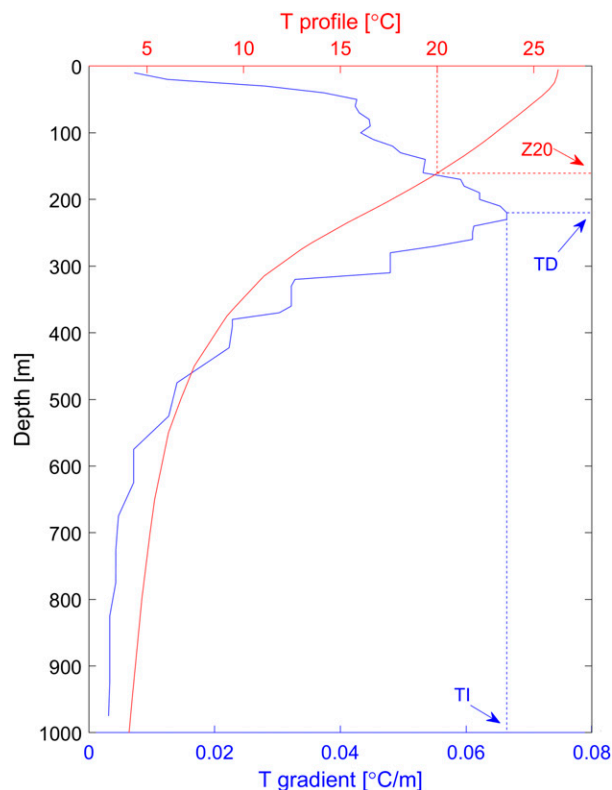


FIG. 1. One example for thermocline depth determination. The red line is the June temperature profile at 20°N, 160°W from EN4, and its vertical gradient is shown by the blue line. The maximum vertical temperature gradient (defined as thermocline depth in this study) is at 220-m depth, which is about 60 m deeper than Z20.

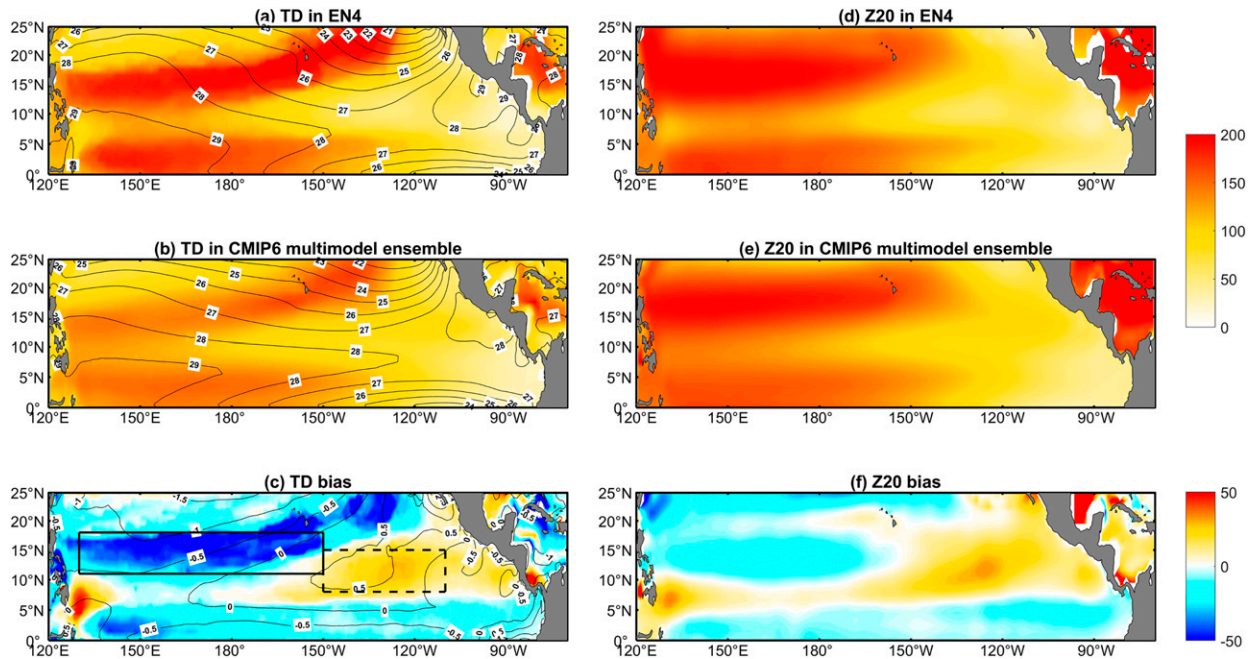


FIG. 2. Annual-mean thermocline depth (color; m) and SST (contours; $^{\circ}\text{C}$) estimated from (a) the observations (EN4 and OISST) and (b) the CMIP6 MME. (c) Annual-mean TD and SST biases of CMIP6 MME relative to the observations. (d)–(f) As in (a)–(c), but for the annual-mean Z20.

greenhouse gases from 1850 to 2014, providing an opportunity to evaluate model ability to simulate the past climate. In our analysis, 50 models are used, and their serial numbers are listed in Table 1. Because the atmospheric products are available since 1979, the last 35 years (1980–2014) of historical simulations are selected for comparison. The selected outputs are interpolated onto a 1° horizontal grid, and the fields of potential temperature and 3D velocities are further interpolated

to 87 standard levels with a vertical resolution of 10 m near the surface and an increase to 200 m at depth.

b. Datasets for model evaluation

To evaluate the thermocline bias in CMIP6 simulations, the version 4 of the Met Office Hadley Centre “EN” series of datasets (EN4; Good et al. 2013) are used for comparison in our study. The EN4 dataset consists of the objective analyses of subsurface ocean temperature and salinity from 1900 to the present, with a 1° horizontal resolution and 42 vertical levels. Atmospheric data are taken from the fifth generation of ECMWF atmospheric reanalyses (ERA5; Copernicus Climate Change Service 2017), with a horizontal resolution of 0.25° from 1979 to the present. Consistent with the preprocessing for CMIP6 simulations, data spanning from 1980 to 2014 are chosen. All datasets are interpolated onto a 1° horizontal grid, and hydrographic data from EN4 are further interpolated to 87 vertical levels.

c. The determination of thermocline depth

The depth of the 20°C isotherm (Z20) is widely used as a proxy of thermocline depth (TD) in the tropical Pacific. However, some studies argue that Z20 is systematically flatter and deeper than the TD along the equator, and the Z20 does not respond correctly to surface wind variations (Castaño-Tierno et al. 2018). In our study, TD for each horizontal grid point is determined by finding the depth at which the vertical temperature gradient has its maximum. One example of TD determination is given in Fig. 1. It is shown that TD is about 60 m deeper than Z20, implying that Z20 is not a good proxy for

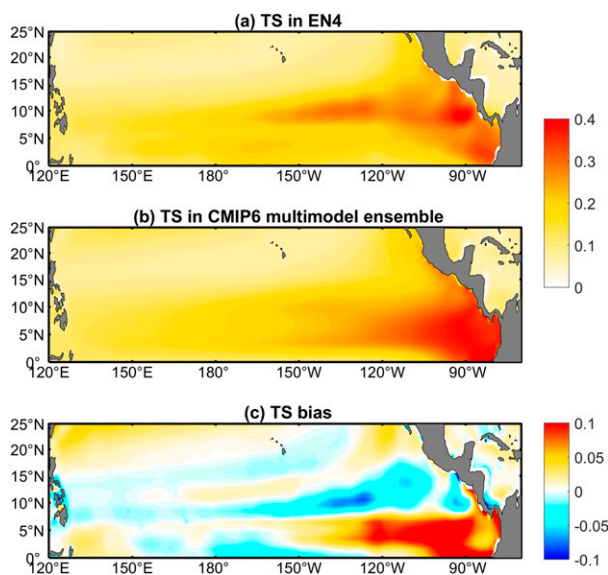


FIG. 3. As in Figs. 2a–c, but for the thermocline strength ($^{\circ}\text{C m}^{-1}$).

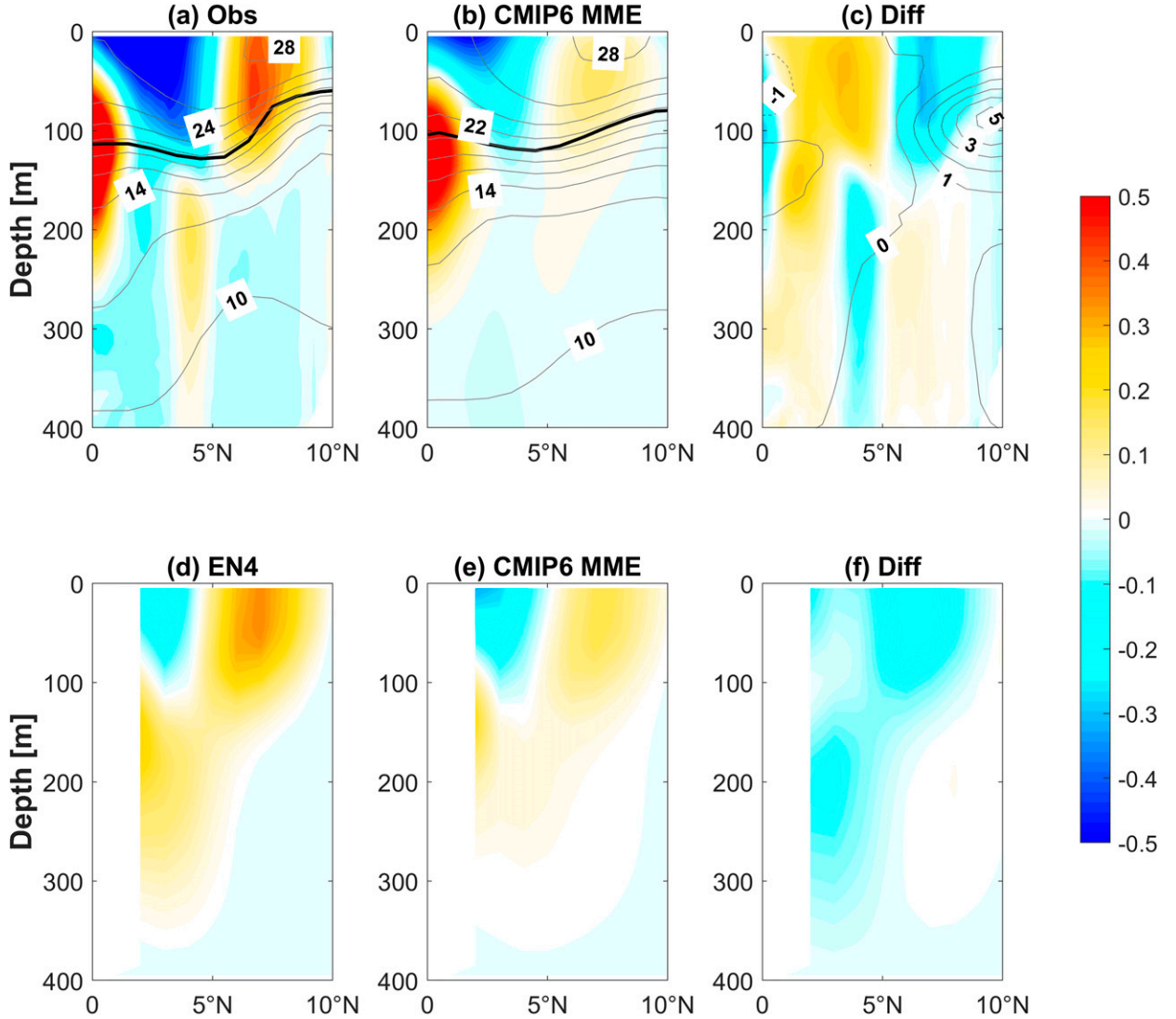


FIG. 4. Annual mean zonal currents (color; m s^{-1}) and temperature (gray contours; $^{\circ}\text{C}$) along 140°W for (a) the observation of Johnson *et al.* (2002) and (b) the CMIP6 MME. (c) Their difference (CMIP6 minus EN4). The black lines in (a) and (b) denote the TD. (d)–(f) As in (a)–(c), but the zonal currents (m s^{-1}) estimated based on the thermal wind relation using the temperature fields from EN4 in (d) and CMIP6 MME in (e).

TD there. In addition, thermocline strength (TS) is defined as the maximum temperature gradient. For example, TS in Fig. 1 is about $6.65 \times 10^{-2} ^{\circ}\text{C m}^{-1}$.

d. Ocean modeling

To investigate the oceanic contribution to thermocline bias in the TNP, MOM5-based ocean-only simulations are also conducted. This ocean model has a nominal 1° horizontal resolution with meridional resolution progressively refined to $1/3^{\circ}$ equatorward of 30° latitude, and 50 vertical levels with 10 m resolution in the upper 220 m. Its vertical mixing scheme consists of three components: a K -profile parameterization for the upper boundary layer, a topographically enhanced mixing scheme for the abyss, and a constant background diffusivity representing the diapycnal mixing in the ocean

interior. More model details can be found in Griffies *et al.* (2009).

e. Fine-scale parameterization

To demonstrate the spatial pattern of diapycnal mixing in the TNP, the field of diapycnal diffusivity is estimated from the strain-based fine-scale parameterization (Kunze *et al.* 2006):

$$K = K_0 \frac{\langle \xi_z^2 \rangle^2}{\text{GM} \langle \xi_z^2 \rangle} h(R_\omega) j(f/N),$$

where $\langle \xi_z^2 \rangle$ is the observed strain variance, $\text{GM} \langle \xi_z^2 \rangle$ is the strain variance from the Garrett–Munk model spectrum, $h(R_\omega)$ is a function of the ratio between shear and strain variance, and $j(f/N)$ is a latitudinal correction given the influence of the

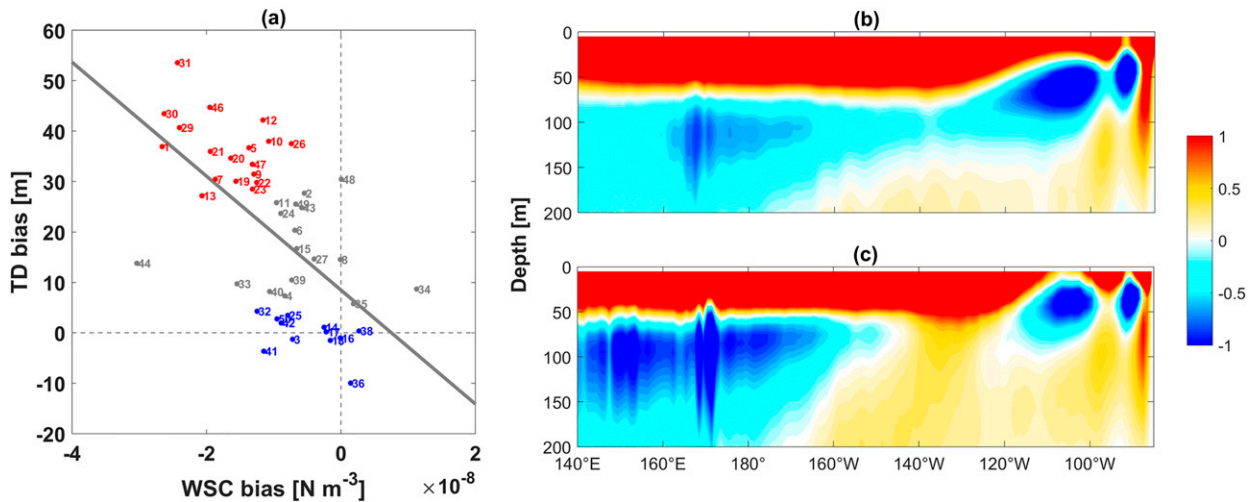


FIG. 5. (a) Scatterplots of the relationship between the biases in WSC and TD over the NETP. Models with a large TD bias are represented by the red dots, while models with a small TD bias are represented by the blue dots. The small numbers next to the circles refer to the numbers listed in Table 1. (b), (c) Zonal-vertical sections of meridional velocity (cm s^{-1}) along 10°N for the models with the large bias and the small bias, respectively.

Coriolis force on the internal wave breaking. To obtain the strain variance, Argo profiles (available online at [ftp://ftp.ifremer.fr/ifremer/argo/](http://ftp.ifremer.fr/ifremer/argo/)) with 2–10-m vertical resolution and from 2006 to 2019 are used. Each selected profile is broken into 256-m half-overlapping segments, and the strain in each segment is calculated and is then integrated in vertical wave-number space to obtain the strain variance. Diffusivity estimates inferred from Argo profiles are grouped into $2^\circ \times 2^\circ$ bins, and the median diffusivity averaged between 250 and 500 m is used to present the diapycnal diffusivity in each bin (at least 10 estimates in each bin to obtain the median).

3. Thermocline simulations in the TNP

Figures 2a and 2b contrast the annual-mean TD in EN4 and CMIP6 multimodel ensemble (MME) respectively, and Fig. 2c shows their annual-mean difference. Compared with the observation, CMIP6 models tend to produce an overly shallow thermocline in the region equatorward of 5°N . This shallow equatorial thermocline bias also exists in CMIP5 models, and some previous studies have attributed the bias to systematic errors in equatorial wind simulation (Li and Xie 2014; Castaño-Tierno et al. 2018). Although it is substantial in magnitude, little attention has been previously placed on the too deep thermocline over the northeastern tropical Pacific (NETP; 8° – 15°N , 110° – 150°W ; dashed black box in Fig. 2c) and the too shallow thermocline over the northwestern tropical Pacific (NWTP; 11° – 18°N , 130°E – 150°W ; solid black box in Fig. 2c). Specifically, the annual-mean TD over the NETP in EN4 is only about 50 m, but that in CMIP6 MME reaches 80 m. In contrast, the TD over the NWTP is about 200 m in EN4, and is shallower than 150 m in CMIP6 MME. In general, although bias in Z20 (Fig. 2f) indicates a similar spatial pattern to that in TD, a great discrepancy in bias magnitude occurs in the NWTP where the TD bias is about 50 m but the Z20 bias is smaller than

20 m, implying that Z20 fails to represent TD in the NWTP (also shown in Fig. 1). Because SST changes are closely coupled with thermocline fluctuations, annual-mean SST bias is also demonstrated in Fig. 2c. Corresponding to the deep thermocline bias, a 0.5°C warm SST bias arises in the NETP. Both the biases in thermocline and SST are related to the wind simulations in the NETP, and more discussion will be given in section 5.

Another important aspect of thermocline representation is its strength. For example, a diffuse thermocline structure along the Pacific equator tends to weaken the sensitivity of SST to anomalous upwelling and vertical mixing (Guilyardi et al. 2009). Figures 3a and 3b compare the annual-mean TS in EN4 and CMIP6 MME. Despite large efforts in model developments over the past decade, diffuse equatorial thermocline bias still persists in the current generation of climate models (Fig. 3c). Besides, TS bias demonstrates a dipole pattern in the NETP, whereas the TS bias is trivial in the NWTP despite the great TD bias there.

4. The influences of the thermocline biases

These thermocline biases can degrade the simulations of oceanic circulations in the tropical Pacific. The North Equatorial Countercurrent (NECC) plays an important role in regulating the tropical Pacific climate (Clement et al. 2005), but it is poorly simulated in many ocean and climate models (Tseng et al. 2016; Sun et al. 2019). For example, ocean models participating in the Coordinated Ocean-ice Reference Experiments produce a NECC whose intensity is approximately half of that observed at 140°W (Tseng et al. 2016). A similar problem is also found in CMIP6 simulations (Figs. 4a–c). The annual mean zonal speed of the NECC in CMIP6 MME is only about 0.1 m s^{-1} (Fig. 4b) compared to the observed $\sim 0.3 \text{ m s}^{-1}$ (Fig. 4a). Volume transport of the NECC is primarily

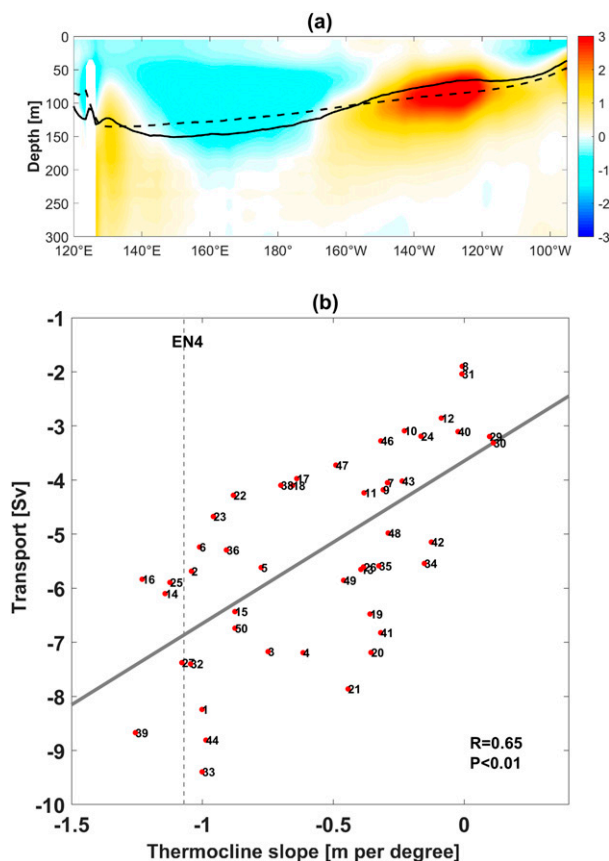


FIG. 6. (a) Depth–longitude section of temperature bias ($^{\circ}\text{C}$; averaged between 5° and 15°N) of CMIP6 MME relative to EN4. Solid and dashed lines indicate the TD estimated from EN4 and CMIP6 MME, respectively. (b) Scatterplots of the relationship between the thermocline slope and volume transport, which is produced as follows. First, TD and meridional velocities are meridionally averaged between 5° and 15°N . Afterward, the trend of the averaged TD shoaling from 145°E to 130°W is used to calculate the thermocline slope; the interior volume transport is estimated by vertically integrating the averaged equatorward meridional velocities from 50 to 250 m and then zonally integrating from 145°E to 130°W . The dashed gray line is the thermocline slope in EN4. The gray solid line is the least squares fit, and the intermodel correlation R is shown in the lower right corner.

controlled by the Sverdrup dynamics (Yu et al. 2000), and hence the biases in meridional derivative of wind stress curl (WSC) and TD would distort the simulation of the NECC. Figures 4d–f demonstrate the zonal currents estimated based on the thermal wind relation ($f\partial u/\partial z = -\alpha g T/\partial y$, where f is the Coriolis parameter and α is the thermal expansion coefficient $-\partial\rho/\rho_0\partial T$; the reference level is 400 m in our calculation). It is shown that the flatter meridional thermocline over the NETP in CMIP6 MME contributes to a weaker NECC as compared with the estimate from EN4 (Fig. 4f).

Another consequence of the shallow TD over the NETP is an influence on the subtropical–tropical water exchange. The ridge-like thermocline in the NETP forms a potential vorticity barrier, which acts to block the local water exchange between

the subtropics and tropics (Lu and McCreary 1995; Johnson and McPhaden 1999). In this way, the flat thermocline bias (Figs. 2c,f) tends to weaken the potential vorticity barrier in the NETP, and can affect the width of subtropical–tropical exchange window. To investigate the relationship between the TD bias and the simulated exchange window width among CMIP6 simulations, we define two model groups according to the magnitude of TD biases (Fig. 5a): 18 models that are seen to have large TD bias, and 12 models that are seen to have trivial or little TD bias. As demonstrated by Figs. 5b and 5c, the models with a great TD bias can produce an equatorward water transport at 100–150 m throughout the basin. But the meridional velocity is mostly poleward between 120° and 160°W in the models with a small TD bias (Fig. 5c), and the equatorward water transport is largely blocked in the NETP.

As the simulated TD is too deep in the NETP and is too shallow in the NWTP (Fig. 2c), the thermocline is also too flat in the zonal direction (Fig. 6a), and the subtropical cells (STCs) in the TNP might be poorly represented. Figure 6b shows the scatterplots of the thermocline slope versus the volume transport between 5° and 15°N . Obviously, these two quantities show a positive correlation ($R = 0.65$), indicating that CMIP6 simulations with the flatter thermocline in the TNP tend to produce a weaker equatorward volume transport in the ocean interior. It is worth noting that the equatorward volume transport is about 6.8 Sv ($1\text{ Sv} \equiv 10^6\text{ m}^3\text{ s}^{-1}$) according to the EN4 thermocline slope if the linear relationship derived from CMIP6 simulations still hold for observations. This value is close to the estimates ($5\text{--}7\text{ Sv}$) in many previous studies (Huang and Liu 1999; Johnson and McPhaden 1999; McPhaden and Zhang 2002). Therefore, the interior volume transport in the TNP is greatly underestimated in most of the CMIP6 simulations. Figure 7a demonstrates the regression map of the intermodel velocities within the thermocline onto the normalized equatorward volume transport. It reveals that the flat thermocline in both the zonal and meridional directions over the NWTP tends to weaken the southwestward volume transport by the STCs, leading to a further decrease in water supply to the Equatorial Undercurrent (EUC). Figure 7b shows a significant negative correlation between the interior transport and the EUC transport at 170°W . However, the EUC is underestimated by $\sim 3.7\text{ Sv}$ in CMIP6 MME, whereas the TNP interior transport seems to be underestimated only by 1.6 Sv . The inconsistency could be due to the fact that the interior transport would move northward along the western boundary and the underestimated TNP interior transport cannot solely explain the too weak EUC. In fact, as the TD bias in the NWTP is primarily caused by the double-ITCZ problem as discussed in the next section, similar WSC and TD biases should also be anchored symmetrically in the southwestern tropical Pacific. Thus, STC errors in southern tropical Pacific might contribute greatly to the EUC bias.

5. Attributions of the thermocline biases

Thermocline fluctuation is strongly influenced by the surface wind stress variation. Thus, we first investigate the contribution of surface wind stress to thermocline bias in the TNP. Figure 8a

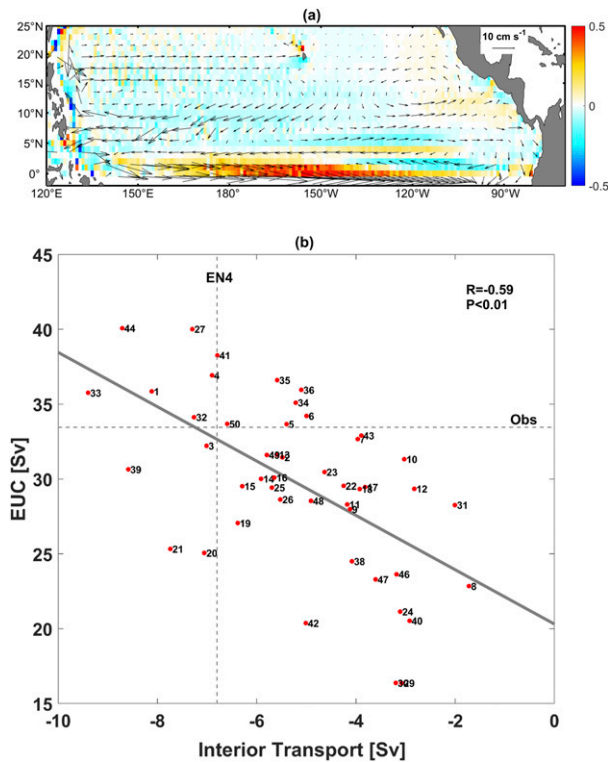


FIG. 7. (a) Linear regressions of the intermodel horizontal (vectors) and vertical (color; m day^{-1}) velocities within the thermocline onto the normalized equatorward volume transport. (b) Scatterplots of the relationship between the interior volume transport and the EUC transport at 170°W . The observed EUC transport is estimated based on the observation of Johnson et al. (2002).

shows the intermodel regressions of wind stress vectors and WSC onto the TD bias in the NWTP. The intermodel differences in the NWTP TD simulations can be explained by the differences in the local WSC simulations. For example, corresponding to a cyclonic WSC bias near 15°N (Fig. 8c) and the resultant Ekman upwelling, TD in CMIP6 models tends to shoal in the NWTP. Similarly, the TD simulations in the NETP also largely depend on the local wind stress simulations (Fig. 8b). The strong northeasterly wind stress bias in the NETP produces a negative curl on its right flank and a positive curl on its left (Fig. 8c), a dipole pattern that is also seen in the TD and TS biases (Figs. 2c and 3c). In addition, the warm SST bias in the NETP (Fig. 2c) is associated with the local wind stress simulations. As shown in Fig. 8c, the southwesterly wind stress bias over $180^\circ\text{--}120^\circ\text{W}$, $5^\circ\text{--}20^\circ\text{N}$ acts to weaken the easterly trade winds and further reduce the upward latent heat flux, eventually leading to the surface warming. Moreover, the southwesterly wind stress bias will produce a negative WSC bias on its right flank. Therefore, both SST bias and TD bias arise in the NETP, but center of the warm SST bias is displaced farther westward. It is interesting to note that regression patterns of wind stress onto the first two principal components of intermodel variability in tropical Pacific precipitation (Li and

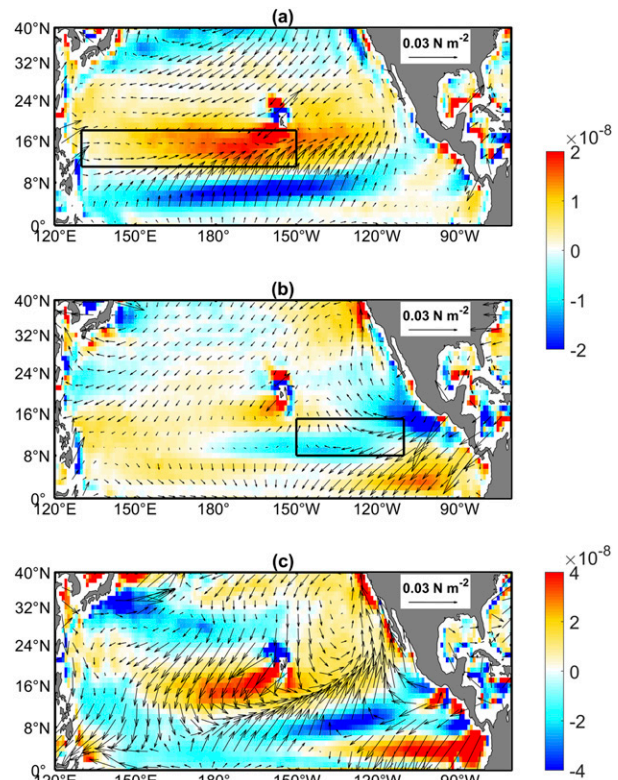


FIG. 8. Linear regressions of the intermodel WSC (color; N m^{-2}) and wind stress vectors (N m^{-2}) onto the normalized (a) NWTP ($11^\circ\text{--}18^\circ\text{N}$, $130^\circ\text{E--}150^\circ\text{W}$) and (b) NETP ($8^\circ\text{--}15^\circ\text{N}$, $110^\circ\text{--}150^\circ\text{W}$) thermocline depth biases, respectively. (c) WSC and wind stress vectors biases relative to ERA5.

Xie 2014) are similar to the patterns shown in Figs. 8a and 8b. Therefore, the thermocline bias can also be traced back to the errors in precipitation simulations.

Intermodel regression analysis is also applied to the annual mean precipitation and sea level pressure (SLP). Associated with the overestimated precipitation near 10°N , low SLP bias centers on the subtropical North Pacific (Figs. 9a,c), resulting in a meridional pressure gradient and the resultant cyclonic WSC bias in the NWTP. These precipitation and SLP biases are part of the double-ITCZ problem. In general, double-ITCZ bias in the western Pacific is controlled by the insufficient atmospheric net energy input near the equator, which is associated with the well-known Pacific cold tongue bias (Adam et al. 2018; Samanta et al. 2019). In contrast, double-ITCZ bias in the eastern Pacific is related to the northeastern Pacific cold bias, which is related to the poor simulations of the North American monsoon in the present climate models (Song and Zhang 2020). Consistent with these studies, CMIP6 models with excessive northeasterly wind stress and large precipitation deficit in the NETP would have a large positive SLP bias in the North America (Figs. 9b,c); these errors eventually lead to the thermocline bias with a dipole pattern in the NETP. Figures 9d–f further show the multimodel scatterplots between the TD biases and their corresponding precipitation biases. It is

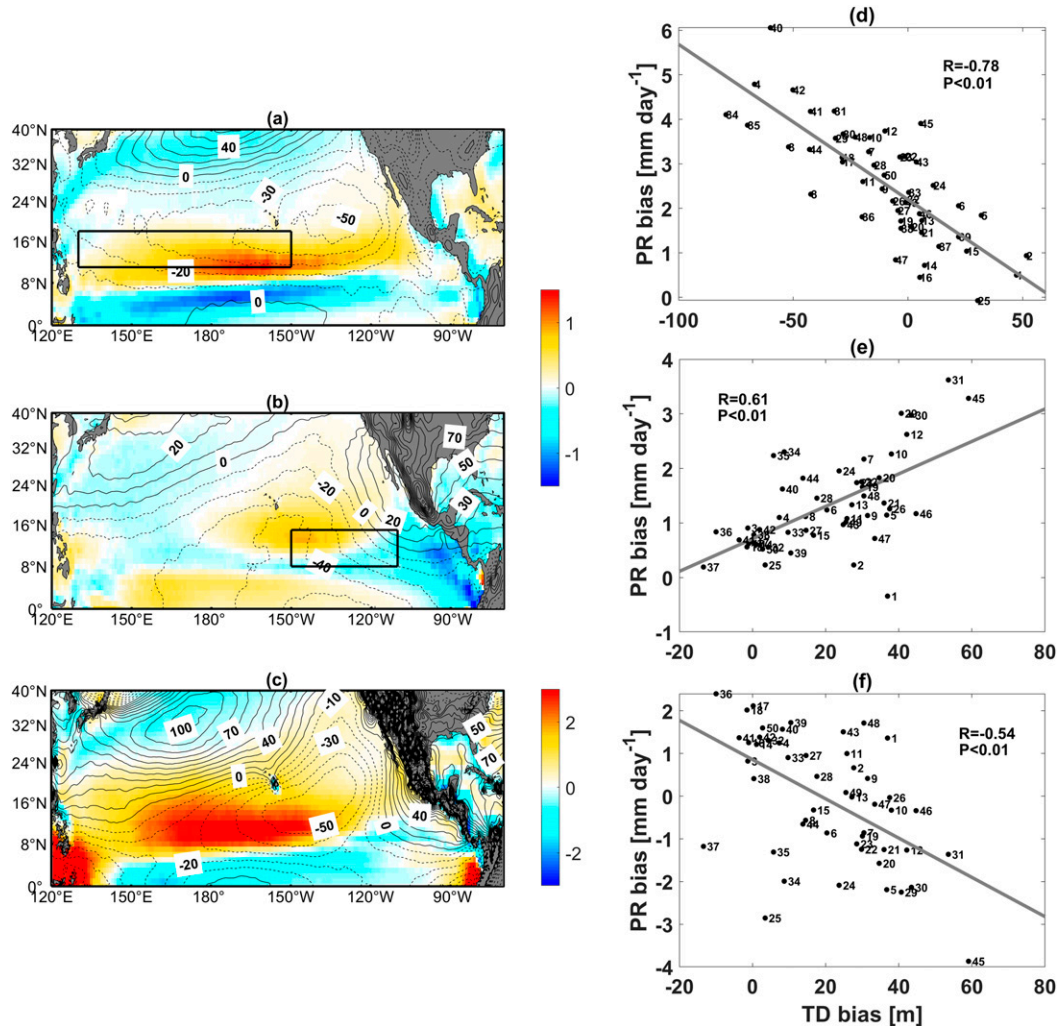


FIG. 9. (a)–(c) As in Fig. 8, but for the annual precipitation (color; mm day⁻¹) and SLP (contours; Pa). (d)–(f) The multimodel scatterplots between the TD biases [in the NWTP in (d); in the NETP in (e) and (f)] and the corresponding precipitation biases [horizontally averaged over 10°–15°N, 155°E–155°W in (d), 13°–20°N, 130°–155°W in (e), and 8°–12°N, 90°–105°W in (f)].

obvious that the CMIP6 simulations with small TD biases tend to produce a better representation of the ITCZ.

It is known that the double-ITCZ bias is seasonally dependent (Adam et al. 2018), and hence the TD bias should vary with seasons as well. Figure 10 shows the seasonality of TD, WSC, and precipitation biases in the TNP. During the second half of a year, the magnitude of the precipitation bias increases (contours in Fig. 10b), and the WSC biases at its north and south flanks both increase correspondingly (color in Fig. 10b). The WSC biases affect the simulations of Ekman pumping in the ITCZ regions, leading to a more pronounced TD bias during June–December (Fig. 10a).

Although these atmospheric factors control the thermocline bias in the TNP, the contributions from ocean processes should be considered as well. Theoretically, when the ocean temperature profile can be fitted by exponential-like solutions and hypothesizing a balance between vertical advection ($w_e \partial T / \partial z$)

and diffusion ($k_v \partial^2 T / \partial z^2$) within the thermocline (Munk 1966), TS is proportional to w_e / k_v , where w_e is the upwelling and k_v is the vertical eddy diffusivity within the thermocline. The w_e is generally caused by the WSC-induced Ekman pumping, and we have investigated its effects above on the oceanic side. The effects of k_v on equatorial TS have been widely investigated in some previous studies (Jochum 2009; Furue et al. 2015; Zhu and Zhang 2018), concluding that reducing the equatorial k_v helps to produce a sharper equatorial thermocline. Thus, some climate models in CMIP6 (e.g., CESM2) take into account the reduced diffusivity near the equator. However, as demonstrated in Fig. 11, k_v is still overestimated in the NETP, being a potential reason for the poorly simulated TS there.

Great uncertainties exist in the parameterizations of oceanic vertical mixing processes, which are considered to be an important source for biases in the ocean simulations (Chen et al. 1994; Fox-Kemper et al. 2019). The observational evidence

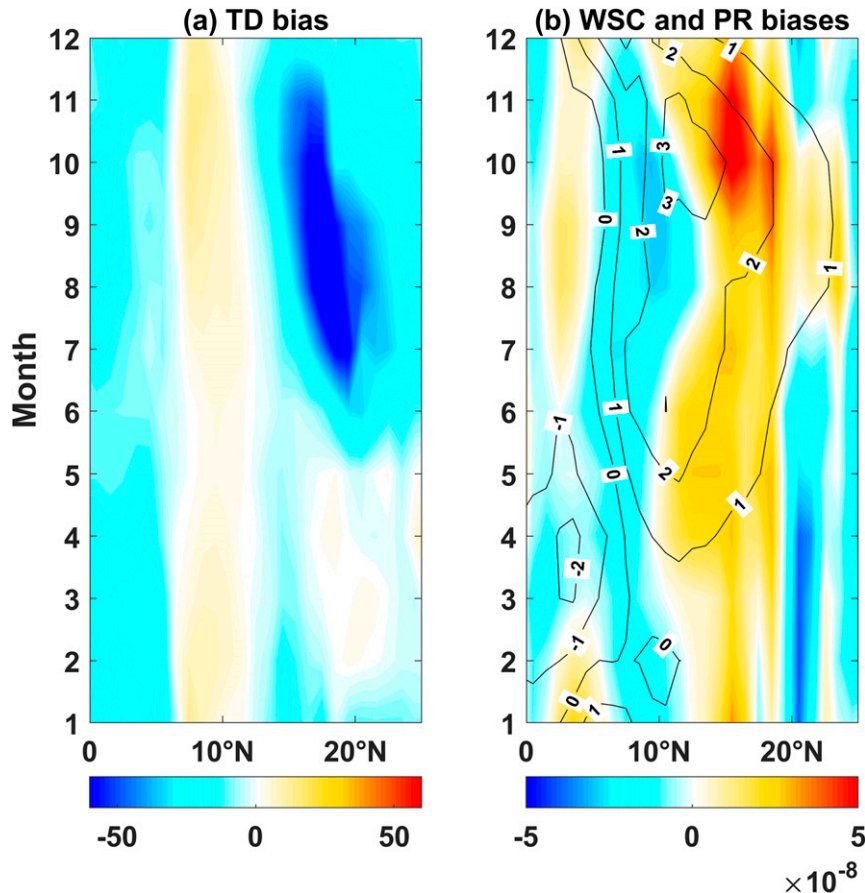


FIG. 10. (a) TD bias (m) and (b) WSC bias (color; N m^{-3}) and precipitation bias (contours; mm day^{-1}) zonally averaged across the basin as a function of calendar month.

shows that near-inertial energy input from winds and eddy kinetic energy in the NETP are lower than those in the midlatitude and, as a consequence, the observed local oceanic diapycnal mixing is weak (Whalen et al. 2018). To investigate the relationship between the thermocline bias and the observed weak diapycnal mixing in the NETP, MOM5-based ocean-only simulations are conducted with two experiments are performed. In the control run, background diffusivity is taken as the commonly used value ($10^{-5} \text{ m}^2 \text{ s}^{-1}$). In the sensitivity run, the background diffusivity over the NETP is replaced by the Argo-derived one (Fig. 11a). Figure 12 presents the differences between the sensitivity run and the control run. In general, the TD differences (Fig. 12a) are not obvious, implying a trivial influence of background diffusivity on the TD in the NETP. However, the thermocline in the NETP is more stratified when the background diffusivity is more realistically prescribed (Fig. 12b), implying that, in addition to the Ekman pumping caused by local WSC, the weak vertical mixing is also an important factor in maintaining the ridge-like thermocline in the NETP.

6. Summary and discussion

The oceanic thermocline is a layer that acts to isolate the upper boundary layer from the deep ocean, and its vertical

displacement is always accompanied by a large change in upper ocean thermal and current structures. Realistic simulation of the thermocline is important for accurate simulations and predictions of climate variability. At present, great thermocline biases still exist in the current generation of climate models. In this study, thermocline biases in the TNP are investigated using the newly released CMIP6 simulations. It is found that CMIP6 models produce an overly shallow thermocline in the NWTP and the region equatorward of 5°N , but produce a deep thermocline in the NETP. Although significant TD bias also arises in the NWTP, large thermocline strength bias only arises in the NETP, which demonstrates a dipole structure centered about 8°N .

The TNP thermocline bias can seriously degrade the simulations of oceanic circulations, including a too weak NECC and a reduction and eastward extension of the equatorward interior water transport. The too weak NECC in CMIP6 models leads to too weak lateral shear instabilities between the NECC and the South Equatorial Current, failing in simulating the observed tropical instability waves (TIWs). By stirring the warm water equatorward, TIWs play an important role in maintaining the heat balance in the eastern tropical Pacific (Kessler et al. 1998; Jochum et al. 2007). Thus, the too weak

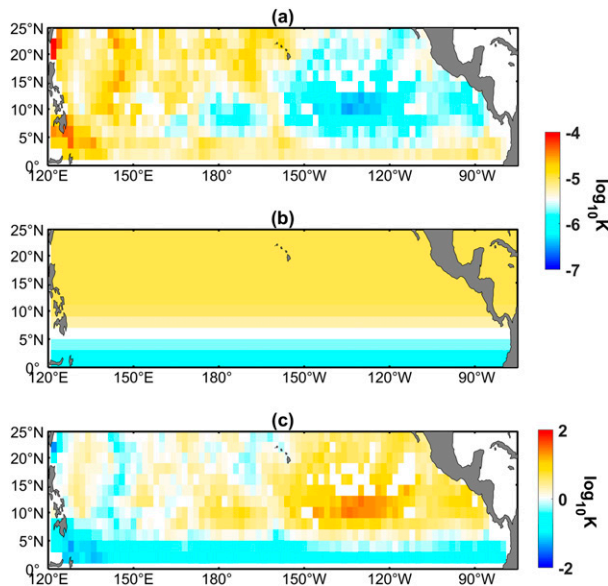


FIG. 11. (a) Diapycnal diffusivity ($\text{m}^2 \text{s}^{-1}$, averaged between 250 and 500 m) estimated based on the fine-scale parameterization (Kunze et al. 2006) using the Argo profiles from 2006 to 2019. (b) The prescribed background diffusivity in CESM2. (c) Their difference (CESM2 minus Argo-derived).

NECC bias is likely to make a contribution to the equatorial too cold tongue bias, and further heat budget analyses are needed to explore this possibility. As demonstrated in Fig. 5, the flat thermocline bias tends to weaken the potential vorticity barrier in the NETP, broaden the subtropical–tropical exchange window, and decrease the equatorward velocity in the NWTP. Thus, the flat thermocline bias weakens the STCs in the TNP. Many previous studies have suggested a strong influence of STCs onto the tropical SST variability. For example, a slowdown of STCs since 1970s has caused a rise in equatorial SST by 0.8°C (McPhaden and Zhang 2002). Similar conclusions still hold for the equatorial SST bias in CMIP6 simulations. CMIP6 models with a large equatorward interior

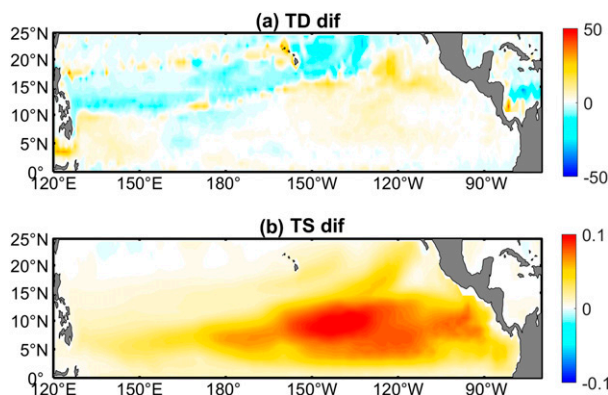


FIG. 12. (a) TD (m) and (b) TS ($^\circ\text{C m}^{-1}$) differences between the sensitivity run and the control run.

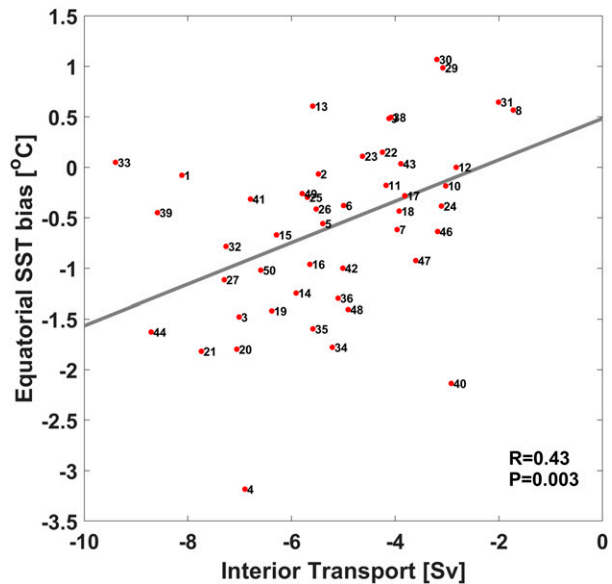


FIG. 13. Scatterplots of the relationship between the interior volume transport and the equatorial SST bias (2°S – 2°N , 180° – 90°W).

transport always have a more serious equatorial cold tongue bias (Fig. 13), and further studies are needed to address this issue quantitatively. In addition, Gu and Philander (1997) propose that the time scale of the tropical Pacific decadal variability (TPDV) is determined by the mean advection of temperature anomalies from the subtropics to the tropics. Therefore, the flat thermocline bias in the TNP has a potential impact on the TPDV. It is hard to explore this relationship using the CMIP6 simulations only, and TPDV should be evaluated under the same model configurations. Thus, further sensitivity experiments with one climate model will be conducted.

Thermocline bias in the TNP is primarily caused by the model deficiency in simulating the surface WSC, which can be further attributed to the longstanding double-ITCZ bias in the TNP. Besides, thermocline bias in the NETP can be partly attributed to the prescription of oceanic background diffusivity. By constraining the diffusivity to match observations, TS in the NETP is greatly increased. The thermocline bias in the TNP is a consequence of the double-ITCZ bias, a persistent problem in climate model simulations. Using the CMIP5 simulations, Xiang et al. (2017) have found that the largest source of the double-ITCZ bias is from atmospheric models. Figure 14 shows the TNP precipitation and WSC biases in CMIP6 and AMIP MME. Consistent with Xiang et al. (2017), the double-ITCZ bias in the NWTP also exists in the AMIP simulations, including an overestimated precipitation and a positive WSC bias over (160°E – 160°W , 10° – 20°N). Through atmospheric general circulation model experiments with different equatorial SST biases prescribed, Samanta et al. (2019) found that this double-ITCZ bias in the atmospheric models can be exacerbated by the Pacific too cold tongue bias. Thus, the double-ITCZ bias in the NWTP is amplified in fully coupled

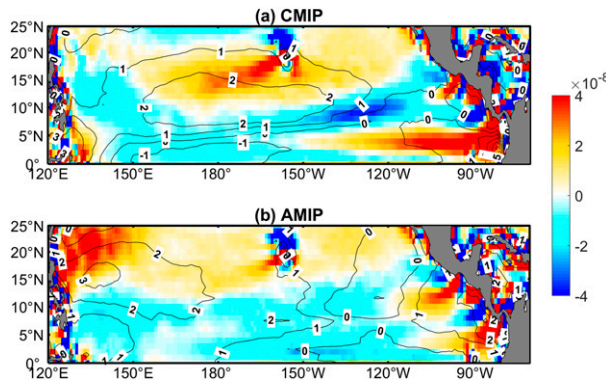


FIG. 14. Precipitation (contours; mm day^{-1}) and WSC (color; N m^{-3}) biases in (a) CMIP6 and (b) AMIP MME.

simulations (Fig. 14a). But in the NETP, CMIP, and AMIP simulations have different bias patterns. In particular, the dipole structure of WSC bias in the CMIP simulations does not appear in the AMIP simulations, implying that the North American monsoon is better captured by atmospheric models but is poorly represented by coupled climate models.

While the thermocline bias in the TNP is a consequence of the double-ITCZ problem and the overestimated precipitation straddles the equator, thermocline bias might be significant in the south tropical Pacific as well. Moreover, considering the fact that the water mass within the Pacific equatorial thermocline is primarily from the Southern Hemisphere (Goodman et al. 2005), tropical climate simulations might be more easily influenced by the thermocline bias in the tropical South Pacific, which will be a subject in our next study.

Finally, it should be cautioned that the reanalysis data are not real observations and sometimes they have large biases themselves. For example, in the present study, the ERA5 wind fields are used to calculate the WSC bias in CMIP6 MME. However, if the wind measurements by QuikSCAT are considered to be more realistic than the ERA5 winds, the resultant patterns of the WSC bias in the TNP are changed greatly (Fig. 15). In fact, it is still unclear which dataset is more reliable for use in ocean modeling. In particular, accuracies of the satellite measurements and reanalysis data will be degraded by rain in the ITCZ region. Thus, more in situ observations are needed to better describe the oceanic and atmospheric state in the TNP.

Acknowledgments. The authors wish to thank the anonymous reviewers for their numerous comments that helped to improve the original manuscript. This research is supported by the National Natural Science Foundation of China [Grants 41906007, 41690122(41690120), 41705082, and 41421005], the National Key Research and Development Program of China [2017YFC1404102(2017YFC1404100)], the Strategic Priority Research Program of Chinese Academy of Sciences (Grants XDB 40000000 and XDB 42000000), and the Shandong Taishan Scholarship. We acknowledge the World Climate Research Programme, which, through its Working Group on Coupled Modelling, coordinated and promoted CMIP6. We

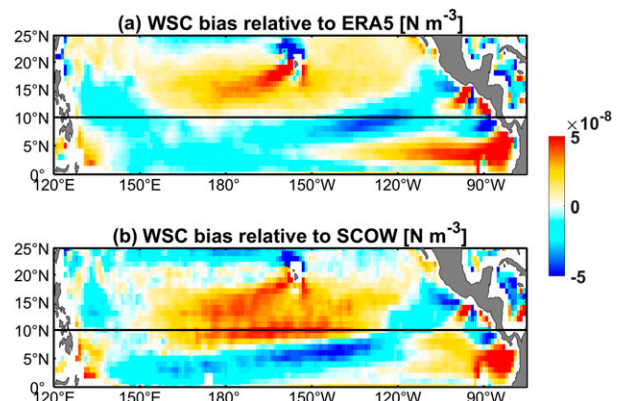


FIG. 15. WSC bias relative to (a) ERA5 and (b) SCOW, respectively. The Scatterometer Climatology of Ocean Winds (SCOW) is estimated from the 122-month record of the QuikSCAT wind measurements (Risien and Chelton 2008), which is available online at <http://cioss.coas.oregonstate.edu/scow/index.html>.

thank the climate modeling groups for producing and making available their model output, the Earth System Grid Federation (ESGF) for archiving the data and providing access, and the multiple funding agencies who support CMIP6 and ESGF.

REFERENCES

- Adam, O., T. Schneider, and F. Briant, 2018: Regional and seasonal variations of the double-ITCZ bias in CMIP5 models. *Climate Dyn.*, **51**, 101–117, <https://doi.org/10.1007/s00382-017-3909-1>.
- Bellenger, H., E. Guilyardi, J. Leloup, M. Lengaigne, and J. Vialard, 2014: ENSO representation in climate models: From CMIP3 to CMIP5. *Climate Dyn.*, **42**, 1999–2018, <https://doi.org/10.1007/s00382-013-1783-z>.
- Burls, N. J., L. Muir, E. M. Vincent, and A. Fedorov, 2017: Extratropical origin of equatorial Pacific cold bias in climate models with links to cloud albedo. *Climate Dyn.*, **49**, 2093–2113, <https://doi.org/10.1007/s00382-016-3435-6>.
- Castano-Tierno, A., E. Mohino, B. Rodríguez-Fonseca, and T. Losada, 2018: Revisiting the CMIP5 thermocline in the equatorial Pacific and Atlantic Oceans. *Geophys. Res. Lett.*, **45**, 12 963–12 971, <https://doi.org/10.1029/2018GL079847>.
- Chen, D., L. M. Rothstein, and A. J. Busalacchi, 1994: A hybrid vertical mixing scheme and its application to tropical ocean models. *J. Phys. Oceanogr.*, **24**, 2156–2179, [https://doi.org/10.1175/1520-0485\(1994\)024<2156:AHVMSA>2.0.CO;2](https://doi.org/10.1175/1520-0485(1994)024<2156:AHVMSA>2.0.CO;2).
- Chen, X. Y., and K.-K. Tung, 2014: Varying planetary heat sink led to global-warming slowdown and acceleration. *Science*, **345**, 897–903, <https://doi.org/10.1126/science.1254937>.
- Clement, A. C., R. Seager, and R. Murtugudde, 2005: Why are there tropical warm pools? *J. Climate*, **18**, 5294–5311, <https://doi.org/10.1175/JCLI3582.1>.
- Copernicus Climate Change Service, 2017: ERA5: Fifth generation of ECMWF atmospheric reanalyses of the global climate. Copernicus Climate Change Service Climate Data Store (CDS), accessed 24 April 2019, <https://cds.climate.copernicus.eu/cdsapp#!/home>.
- de Szoeke, S. P., and S.-P. Xie, 2008: The tropical eastern Pacific seasonal cycle: Assessment of errors and mechanisms in IPCC

- AR4 coupled ocean–atmosphere general circulation models. *J. Climate*, **21**, 2573–2590, <https://doi.org/10.1175/2007JCLI1975.1>.
- Eyring, V., S. Bony, G. A. Meehl, C. A. Senior, B. Stevens, R. J. Stouffer, and K. E. Taylor, 2016: Overview of the Coupled Model Intercomparison Project Phase 6 (CMIP6) experimental design and organization. *Geosci. Model Dev.*, **9**, 1937–1958, <https://doi.org/10.5194/gmd-9-1937-2016>.
- Fox-Kemper, B., and Coauthors, 2019: Challenges and prospects in ocean circulation models. *Front. Mar. Sci.*, **6**, 65, <https://doi.org/10.3389/fmars.2019.00065>.
- Furue, R., and Coauthors, 2015: Impacts of regional mixing on the temperature structure of the equatorial Pacific Ocean. Part I: Vertically uniform vertical diffusion. *Ocean Modell.*, **91**, 91–111, <https://doi.org/10.1016/j.ocemod.2014.10.002>.
- Good, S. A., M. J. Martin, and N. A. Rayner, 2013: EN4: Quality controlled ocean temperature and salinity profiles and monthly objective analyses with uncertainty estimates. *J. Geophys. Res. Oceans*, **118**, 6704–6716, <https://doi.org/10.1002/2013JC009067>.
- Goodman, P. J., W. Hazeleger, P. de Vries, and M. Cane, 2005: Pathways into the Pacific Equatorial Undercurrent: A trajectory analysis. *J. Phys. Oceanogr.*, **35**, 2134–2151, <https://doi.org/10.1175/JPO2825.1>.
- Griffies, S. M., and Coauthors, 2009: Coordinated Ocean-ice Reference Experiments (COREs). *Ocean Modell.*, **26** (1–2), 1–46, <https://doi.org/10.1016/j.ocemod.2008.08.007>.
- Gu, D., and S. G. H. Philander, 1997: Interdecadal climate fluctuations that depend on exchanges between the tropics and extratropics. *Science*, **275**, 805–807, <https://doi.org/10.1126/science.275.5301.805>.
- Guilyardi, E., A. Wittenberg, A. Fedorov, M. Collins, C. Wang, A. Capotondi, G. J. van Oldenborgh, and T. Stockdale, 2009: Understanding El Niño in ocean–atmosphere general circulation models: Progress and challenges. *Bull. Amer. Meteor. Soc.*, **90**, 325–340, <https://doi.org/10.1175/2008BAMS2387.1>.
- Huang, B., and Z. Liu, 1999: Pacific subtropical–tropical thermocline water exchange in the National Centers for Environmental Prediction ocean model. *J. Geophys. Res.*, **104**, 11 065–11 076, <https://doi.org/10.1029/1999JC900024>.
- Jochum, M., 2009: Impact of latitudinal variations in vertical diffusivity on climate simulations. *J. Geophys. Res.*, **114**, C01010, <https://doi.org/10.1029/2008JC005030>.
- , M. F. Cronin, W. S. Kessler, and D. Shea, 2007: Observed horizontal temperature advection by tropical instability waves. *Geophys. Res. Lett.*, **34**, L09604, <https://doi.org/10.1029/2007GL029416>.
- Johnson, G. C., and M. J. McPhaden, 1999: Interior pycnocline flow from the subtropical to the equatorial Pacific Ocean. *J. Phys. Oceanogr.*, **29**, 3073–3089, [https://doi.org/10.1175/1520-0485\(1999\)029<3073:IPFFTS>2.0.CO;2](https://doi.org/10.1175/1520-0485(1999)029<3073:IPFFTS>2.0.CO;2).
- , B. M. Sloyan, W. S. Kessler, and K. E. McTaggart, 2002: Direct measurements of upper ocean currents and water properties across the tropical Pacific during the 1990s. *Prog. Oceanogr.*, **52**, 31–61, [https://doi.org/10.1016/S0079-6611\(02\)00021-6](https://doi.org/10.1016/S0079-6611(02)00021-6).
- Kessler, W. S., L. M. Rothstein, and D. Chen, 1998: The annual cycle of SST in the eastern tropical Pacific, diagnosed in an ocean GCM. *J. Climate*, **11**, 777–799, [https://doi.org/10.1175/1520-0442\(1998\)011<0777:TACOSI>2.0.CO;2](https://doi.org/10.1175/1520-0442(1998)011<0777:TACOSI>2.0.CO;2).
- Kunze, E., E. Firing, J. M. Hummon, T. K. Chereskin, and A. M. Thurnherr, 2006: Global abyssal mixing inferred from lowered ADCP shear and CTD strain profiles. *J. Phys. Oceanogr.*, **36**, 1553–1576, <https://doi.org/10.1175/JPO2926.1>.
- Li, G., and S.-P. Xie, 2014: Tropical biases in CMIP5 multimodel ensemble: The excessive equatorial Pacific cold tongue and double ITCZ problems. *J. Climate*, **27**, 1765–1780, <https://doi.org/10.1175/JCLI-D-13-00337.1>.
- Li, X., Z.-Z. Hu, B. Huang, and F.-F. Jin, 2020: On the interdecadal variation of the warm water volume in the tropical Pacific around 1999/2000. *J. Geophys. Res. Atmos.*, **125**, e2020JD033306, <https://doi.org/10.1029/2020JD033306>.
- Lohmann, K., and M. Latif, 2005: Tropical Pacific decadal variability and the subtropical–tropical cells. *J. Climate*, **18**, 5163–5178, <https://doi.org/10.1175/JCLI3559.1>.
- Lu, P., and J. P. McCreary, 1995: Influence of the ITCZ on the flow of thermocline water from the subtropical to the equatorial Pacific Ocean. *J. Phys. Oceanogr.*, **25**, 3076–3088, [https://doi.org/10.1175/1520-0485\(1995\)025<3076:IOTIOT>2.0.CO;2](https://doi.org/10.1175/1520-0485(1995)025<3076:IOTIOT>2.0.CO;2).
- McPhaden, M. J., and D. Zhang, 2002: Slowdown of the meridional overturning circulation in the upper Pacific Ocean. *Nature*, **415**, 603–608, <https://doi.org/10.1038/415603a>.
- Meehl, G. A., P. R. Gent, J. M. Arblaster, B. L. Otto-Bliesner, E. C. Brady, and A. Craig, 2001: Factors that affect the amplitude of El Niño in global coupled climate models. *Climate Dyn.*, **17**, 515–526, <https://doi.org/10.1007/PL00007929>.
- Munk, W. H., 1966: Abyssal recipes. *Deep-Sea Res. Oceanogr. Abstr.*, **13**, 707–730, [https://doi.org/10.1016/0011-7471\(66\)90602-4](https://doi.org/10.1016/0011-7471(66)90602-4).
- Nagura, M., W. Sasaki, T. Tozuka, J.-J. Luo, S. K. Behera, and T. Yamagata, 2013: Longitudinal biases in the Seychelles Dome simulated by 35 ocean–atmosphere coupled general circulation models. *J. Geophys. Res. Oceans*, **118**, 831–846, <https://doi.org/10.1029/2012JC008352>.
- Richter, I., 2015: Climate model biases in the eastern tropical oceans: Causes, impacts and ways forward. *Wiley Interdiscip. Rev.: Climate Change*, **6**, 345–358, <https://doi.org/10.1002/wcc.338>.
- , and H. Tokinaga, 2020: An overview of the performance of CMIP6 models in the tropical Atlantic: Mean state, variability, and remote impacts. *Climate Dyn.*, **55**, 2579–2601, <https://doi.org/10.1007/s00382-020-05409-w>.
- , S.-P. Xie, S. K. Behera, T. Doi, and Y. Masumoto, 2014: Equatorial Atlantic variability and its relation to mean state biases in CMIP5. *Climate Dyn.*, **42**, 171–188, <https://doi.org/10.1007/s00382-012-1624-5>.
- Risien, C. M., and D. B. Chelton, 2008: A global climatology of surface wind and wind stress fields from eight years of QuikSCAT scatterometer data. *J. Phys. Oceanogr.*, **38**, 2379–2413, <https://doi.org/10.1175/2008JPO3881.1>.
- Rothstein, L. M., R.-H. Zhang, A. J. Busalacchi, and D. Chen, 1998: A numerical simulation of the mean water pathways in the subtropical and tropical Pacific Ocean. *J. Phys. Oceanogr.*, **28**, 322–343, [https://doi.org/10.1175/1520-0485\(1998\)028<0322:ANSOTM>2.0.CO;2](https://doi.org/10.1175/1520-0485(1998)028<0322:ANSOTM>2.0.CO;2).
- Samanta, D., K. B. Karnauskas, and N. F. Goodkin, 2019: Tropical Pacific SST and ITCZ biases in climate models: Double trouble for future rainfall projections? *Geophys. Res. Lett.*, **46**, 2242–2252, <https://doi.org/10.1029/2018GL081363>.
- Song, F., and G. J. Zhang, 2020: The impacts of horizontal resolution on the seasonally dependent biases of the northeastern Pacific ITCZ in coupled climate models. *J. Climate*, **33**, 941–957, <https://doi.org/10.1175/JCLI-D-19-0399.1>.
- Sun, Z., H. Liu, P. Lin, Y. Tseng, J. Small, and F. Bryan, 2019: The modeling of the North Equatorial Countercurrent in the Community Earth System Model and its oceanic component.

- J. Adv. Model. Earth Syst.*, **11**, 531–544, <https://doi.org/10.1029/2018MS001521>.
- Tatebe, H., and H. Hasumi, 2010: Formation mechanism of the Pacific equatorial thermocline revealed by a general circulation model with a high accuracy tracer advection scheme. *Ocean Modell.*, **35**, 245–252, <https://doi.org/10.1016/j.ocemod.2010.07.011>.
- Thomas, M. D., and A. V. Fedorov, 2017: The eastern subtropical Pacific origin of the equatorial cold bias in climate models: A Lagrangian perspective. *J. Climate*, **30**, 5885–5900, <https://doi.org/10.1175/JCLI-D-16-0819.1>.
- Tseng, Y., and Coauthors, 2016: North and equatorial Pacific Ocean circulation in the CORE-II hindcast simulations. *Ocean Modell.*, **104**, 143–170, <https://doi.org/10.1016/j.ocemod.2016.06.003>.
- Wang, C., L. Zhang, S.-K. Lee, L. Wu, and C. R. Mechoso, 2014: A global perspective on CMIP5 climate model biases. *Nat. Climate Change*, **4**, 201–205, <https://doi.org/10.1038/nclimate2118>.
- Whalen, C. B., J. A. MacKinnon, and L. D. Talley, 2018: Large-scale impacts of the mesoscale environment on mixing from wind-driven internal waves. *Nat. Geosci.*, **11**, 842–847, <https://doi.org/10.1038/s41561-018-0213-6>.
- Xiang, B., B. Wang, Q. Ding, F.-F. Jin, X. Fu, and H.-J. Kim, 2012: Reduction of the thermocline feedback associated with mean SST bias in ENSO simulation. *Climate Dyn.*, **39**, 1413–1430, <https://doi.org/10.1007/s00382-011-1164-4>.
- , M. Zhao, I. M. Held, and J.-C. Golaz, 2017: Predicting the severity of spurious “double ITCZ” problem in CMIP5 coupled models from AMIP simulations. *Geophys. Res. Lett.*, **44**, 1520–1527, <https://doi.org/10.1002/2016GL071992>.
- Xu, Z., M. Li, C. M. Patricola, and P. Chang, 2014: Oceanic origin of southeast tropical Atlantic biases. *Climate Dyn.*, **43**, 2915–2930, <https://doi.org/10.1007/s00382-013-1901-y>.
- Yu, Z., J. P. M. Jr, W. S. Kessler, and K. A. Kelly, 2000: Influence of equatorial dynamics on the Pacific North Equatorial Countercurrent. *J. Phys. Oceanogr.*, **30**, 3179–3190, [https://doi.org/10.1175/1520-0485\(2000\)030<3179:IOEDOT>2.0.CO;2](https://doi.org/10.1175/1520-0485(2000)030<3179:IOEDOT>2.0.CO;2).
- Zhang, R.-H., and A. J. Busalacchi, 1999: A possible link between off-equatorial warm anomalies propagating along the NECC path and the onset of the 1997–98 El Niño. *Geophys. Res. Lett.*, **26**, 2873–2876, <https://doi.org/10.1029/1999GL002315>.
- , L. M. Rothstein, and A. J. Busalacchi, 1998: Origin of upper-ocean warming and El Niño change on decadal scales in the tropical Pacific Ocean. *Nature*, **391**, 879–883, <https://doi.org/10.1038/36081>.
- , T. Takashi, and S. E. Zebiak, 2001: Subduction of decadal North Pacific thermal anomalies in an ocean GCM. *Geophys. Res. Lett.*, **28**, 2449–2452, <https://doi.org/10.1029/2000GL012779>.
- , and Coauthors, 2020: A review of progress in coupled ocean–atmosphere model developments for ENSO studies in China. *J. Oceanol. Limnol.*, **38**, 930–961, <https://doi.org/10.1007/s00343-020-0157-8>.
- Zheng, X.-T., L. Gao, G. Li, and Y. Du, 2016: The Southwest Indian Ocean thermocline dome in CMIP5 models: Historical simulation and future projection. *Adv. Atmos. Sci.*, **33**, 489–503, <https://doi.org/10.1007/s00376-015-5076-9>.
- Zhu, Y., and R.-H. Zhang, 2018: An Argo-derived background diffusivity parameterization for improved ocean simulations in the tropical Pacific. *Geophys. Res. Lett.*, **45**, 1509–1517, <https://doi.org/10.1002/2017GL076269>.
- , and —, 2019: A modified vertical mixing parameterization for its improved ocean and coupled simulations in the tropical Pacific. *J. Phys. Oceanogr.*, **49**, 21–37, <https://doi.org/10.1175/JPO-D-18-0100.1>.
- , —, and J. Sun, 2020: North Pacific upper-ocean cold temperature biases in CMIP6 simulations and the role of regional vertical mixing. *J. Climate*, **33**, 7523–7538, <https://doi.org/10.1175/JCLI-D-19-0654.1>.
- Zuidema, P., and Coauthors, 2016: Challenges and prospects for reducing coupled climate model SST biases in the eastern tropical Atlantic and Pacific Oceans: The U.S. CLIVAR Eastern Tropical Oceans Synthesis Working Group. *Bull. Amer. Meteor. Soc.*, **97**, 2305–2328, <https://doi.org/10.1175/BAMS-D-15-00274.1>.